



Enhancing the performance of green solid-state electric double-layer capacitor incorporated with fumed silica nanoparticles

Mee Yoke Chong^{a,b}, Arshid Numan^{a,**}, Chiam-Wen Liew^c, H.M. Ng^a, K. Ramesh^a, S. Ramesh^{a,*}

^a Centre for Ionics University of Malaya, Department of Physics, Faculty of Science, University of Malaya, 50603 Kuala Lumpur, Malaysia

^b Centre of American Education, INTI International University, Persiaran Bandar Baru Nilai, 71800 Nilai, Malaysia

^c Department of Physical Science, Faculty of Applied Sciences, Tunku Abdul Rahman University College, Jalan Genting Kelang, Setapak, 53300 Kuala Lumpur, Malaysia

ARTICLE INFO

Keywords:

Fumed-silica nanoparticles
Hydroxylethyl cellulose
Solution casting
Thin film
Electrochemical properties

ABSTRACT

Solid polymer electrolyte (SPE) based on fumed silica nanoparticles as nanofillers, hydroxylethyl cellulose (HEC) as host polymer, magnesium trifluoromethanesulfonate salt and 1-ethyl-3-methylimidazolium trifluoromethanesulfonate ionic liquid is prepared by solution casting technique. The ionic conductivity, interactions of adsorbed ions on the host polymer, structural crystallinity and thermal stability are evaluated by electrochemical impedance spectroscopy (EIS), Fourier transform infrared spectroscopy (FTIR), X-ray diffraction (XRD) and thermogravimetric analysis (TGA), respectively. Ionic conductivity studies at room temperature reveals that the SPE with 2 wt. % of fumed silica nanoparticles gives the highest conductivity compared to its counterpart. The XRD and FTIR studies confirm the dissolution of salt, ionic liquid and successful incorporation of fumed silica nanoparticles with host polymer. In order to examine the performance of SPEs, electric double-layer capacitor (EDLC) are fabricated by using activated carbon electrodes. EDLC studies demonstrate that SPE incorporated with 2 wt. % fumed silica nanoparticles gives high specific capacitance (25.0 F/g) at a scan rate of 5 mV/s compared to SPE without fumed silica. Additionally, it is able to withstand 71.3% of capacitance from its initial capacitance value over 1600 cycles at a current density of 0.4 A/g.

1. Introduction

In this modern era, the usage of electronic and electrical equipment is increasing dramatically, which created the alarming issues of managing and disposing of electronic as well as electrical waste (e-waste). The e-waste generated from the use of cell phone became the second highest contributor to the total e-waste in accordance to the European Union Directive [1]. Moreover, hazardous materials such as heavy metals (i.e. copper, aluminium, chromium, lead, mercury, etc.), flame retardants, plastic casings and energy storage devices (i.e. batteries and supercapacitor) are produced from the e-waste of cell phone [2]. Consequently, the managing and disposal of huge volume of e-waste and the release of numerous hazardous materials (flame retardants and heavy metals) may pose a threat to the environment and human health [3,4]. Therefore, materials (heavy metals from the flame retardants plastic casings) recovery was adopted to reduce the discharge of harmful wastes to the environment [5]. However, in order to manage e-waste and to reduce its dumping space, biodegradable energy storage devices are

critically needed as an alternative of conventional energy storage devices for latest technological equipment.

Batteries and supercapacitors are the most commonly used energy storage devices in the cell phone, laptops and other portable electronic devices. Supercapacitors (electrochemical capacitors or ultracapacitors) gained its popularity since 1800 owing to its higher power and energy densities than batteries and conventional capacitors, respectively [6]. Supercapacitors are categorized into pseudocapacitors and EDLCs according to their charge storage mechanism [7]. An EDLC has more influential advantages such as larger specific capacitance, higher specific power and longer life cycle than a pseudocapacitor [8]. On top of that, EDLC have an additional feature that is environmental friendly by using various natural and synthetic biodegradable polymers namely chitosan, starch, iota(i)-carrageenan, xanthan gum, cellulose derivatives and poly(vinyl alcohol) (PVA) were utilized as the host polymers for EDLCs [9,10].

Herein, EDLC based on biodegradable SPE has been fabricated using HEC as host polymer. HEC has many electron-donating atoms per

* Corresponding author.

** Corresponding author.

E-mail addresses: numan.arshed@yahoo.com (A. Numan), rameshtsubra@gmail.com (S. Ramesh).

Table 1

Compositions and designations for HEC: MgTf₂: EMIMTf: fumed silica complexes.

Compositions (wt. %) HEC: MgTf ₂ : EMIMTf: Fumed silica	Designations
36.0: 24.0: 40.0: 0.0	HE40
47.2: 11.8: 40.0: 1.0	HS1
46.4: 11.6: 40.0: 2.0	HS2
45.6: 11.4: 40.0: 3.0	HS3
44.8: 11.2: 40.0: 4.0	HS4

monomer that provide spaces for the adsorption of charge carriers through ion-dipole interaction. Subsequently, it fulfills the most important criteria of a polymer electrolyte that is high ionic conductivity and charge storage capacity which makes it suitable candidate for energy storage applications. On top of that, HEC is a green material with excellent solubility in water, biocompatibility, easy availability, low cost and nonionic behavior [11,12].

However, supercapacitors fabricated by biodegradable SPE comprising of HEC as host polymer and magnesium trifluoromethanesulfonate (MgTf₂) salt suffers from low ionic conductivity at room temperature ($\sim 10^{-9}$ to $\sim 10^{-7}$ S/cm) even though it has outstanding features such as compact structure with no leakage problem, low flammability, good flexibility, safety, stable contact between the electrode and electrolyte [13]. Therefore, ionic liquids are employed to enhance the conductivity of SPEs. They offer wider potential window, high electric conductivity and excellent thermal stability. Herein, 1-ethyl-3-methylimidazolium trifluoromethanesulfonate (EMIMTf) ionic liquid (IL) is used to improvise the conductivity of the SPE.

Besides IL, metal oxide nanoparticles as nanofillers can play significant role in boosting the mechanical strength and ionic conductivity of SPE by interacting with mobile ions. Fumed silica (SiO₂) nanoparticles has been chosen as filler in this study owing to their large contact surface area and amorphosity [14]. According to Kim et al. (2003), these nanoparticles are able to create better adsorption with both host polymer and salt through hydrogen bonding due to its reactive silanol (Si-OH) groups [15]. Thus, it leads to the superior interfacial stability due to which it is widely used as reinforcing nanofiller for silicon rubber, high and low temperature resistant elastomer (in wires, cables and automotive components) and thermal insulation materials, thickening and anti-setting agents in liquid systems (coatings, adhesives, printing inks, cosmetics, foods and fire extinguisher powders) [16,17].

Based on the above facts, SPEs (with and without fumed silica nanoparticles) were prepared and these SPEs were characterized by using EIS, XRD, TGA and FTIR. The performance of the SPEs towards the EDLC is evaluated by using cyclic voltammetry (CV), galvanostatic charge-discharge (GCD) and EIS. It was found that the introduction of fumed silica nanoparticles into the SPE not only enhanced the ionic conductivity and thermal stability, but also facilitated the better penetration and entrapment of ions into the bulk electrodes.

2. Experimental

2.1. Materials

Activated carbon (AC) BP20 and N-methyl-2-pyrrolidone (NMP) (Purity 99.5%) were obtained from Kuraray Chemical Co. Ltd., Japan and Merck, Germany, respectively. HEC, MgTf₂, EMIMTf, fumed silica nanoparticles, carbon black (Super P) and poly(vinylidene fluoride) (PVdF) were purchased from Sigma-Aldrich, USA. Deionized water (DI) was used for the preparation of aqueous solutions.

2.2. Preparation of biodegradable nanocomposites SPE

Fumed silica nanoparticle were activated by the method reported by Taghizadeh and Aghjekohal (2015) [18]. HEC, MgTf₂ and activated

fumed silica nanoparticles were pre-heated for 1 h at 100 °C to remove moisture. After that, HEC, MgTf₂, EMIMTf and different wt. % of activated fumed silica nanoparticles (presented in Table 1) were mixed in DI using bath sonication for 30 min followed by constant stirring for 24 h at room temperature. Finally, the homogeneous slurry was cast on a Teflon coated aluminum foil and allowed to evaporate at 70 °C. After drying, a thin solid film of polymer electrolyte was obtained.

2.3. Characterizations of SPE

Ionic conductivity was measured using an AC impedance technique using HIOKI 3532-50 LCR HiTESTER, over a frequency range from 50 to 1000,000 Hz and temperature range of 30–120 °C. SPE films were mounted on the holder with stainless steel (SS) blocking electrodes under spring pressure with the configuration of SS/SPE/SS blocking electrodes. Bulk resistance was obtained from the complex impedance plots of the SPE. The ionic conductivity (σ), and the activation energy (E_a) of the SPE complexes was calculated by the following equations:

$$\sigma = \frac{d}{R_b A} \quad (1)$$

where “d” is thickness of film (cm), “R_b” is bulk resistance obtained from Cole-Cole plot (Ω), and “A” is the area of the film (cm²).

$$\sigma_T = \sigma_o \exp\left(\frac{-E_a}{kT}\right) \quad (2)$$

where “ σ_T ” is the ionic conductivity at different temperature, “ σ_o ” is the conductivity pre-exponential factor, “k” is the Boltzmann constant, “ E_a ” is the activation energy and “T” is the absolute temperature.

Complex impedance data, Z^* , can be represented by its real, Z' , and imaginary, Z'' , parts by the relation

$$Z^* = Z' - jZ'' \quad (3)$$

where $Z' = |Z| \cos \theta$, $Z'' = |Z| \sin \theta$ and j is constant.

The equations for the dielectric permittivity, ϵ' , the dielectric loss, ϵ'' , the real modulus, M' , and the imaginary modulus M'' can be illustrated as

$$\epsilon' = \frac{Z''}{\omega C_o [(Z')^2 + (Z'')^2]} \quad (4)$$

$$\epsilon'' = \frac{Z'}{\omega C_o [(Z')^2 + (Z'')^2]} \quad (5)$$

$$M' = \frac{\epsilon'}{[(\epsilon')^2 + (\epsilon'')^2]} \quad (6)$$

$$M'' = \frac{\epsilon''}{[(\epsilon')^2 + (\epsilon'')^2]} \quad (7)$$

FTIR studies were conducted by using Themoscscientific Nicolet iS10 FTIR spectrometer which was equipped with an internal reflection accessory. The resolution of the spectrum was 4 cm⁻¹ in the wavenumber region between 4000 cm⁻¹ and 400 cm⁻¹ recorded in the transmittance mode. XRD patterns of SPEs were measured using Siemens D5000 diffractometer with Cu-K α radiation ($\lambda = 1.5406 \text{ \AA}$) and thermal properties were studied using TGA Q500 V20.13 Build 39 (TA, Instruments, New Castle, DE, USA) with a temperature up to 800 °C.

2.4. Preparation of electrode

The ink for the fabrication of the electrode was prepared by mixing 80 wt. % of activated carbon, 10 wt. % of carbon black and 10 wt. % of PVdF binder in NMP solvent under ultrasonication. The mixture was constantly stirred overnight at ambient temperature until homogenous

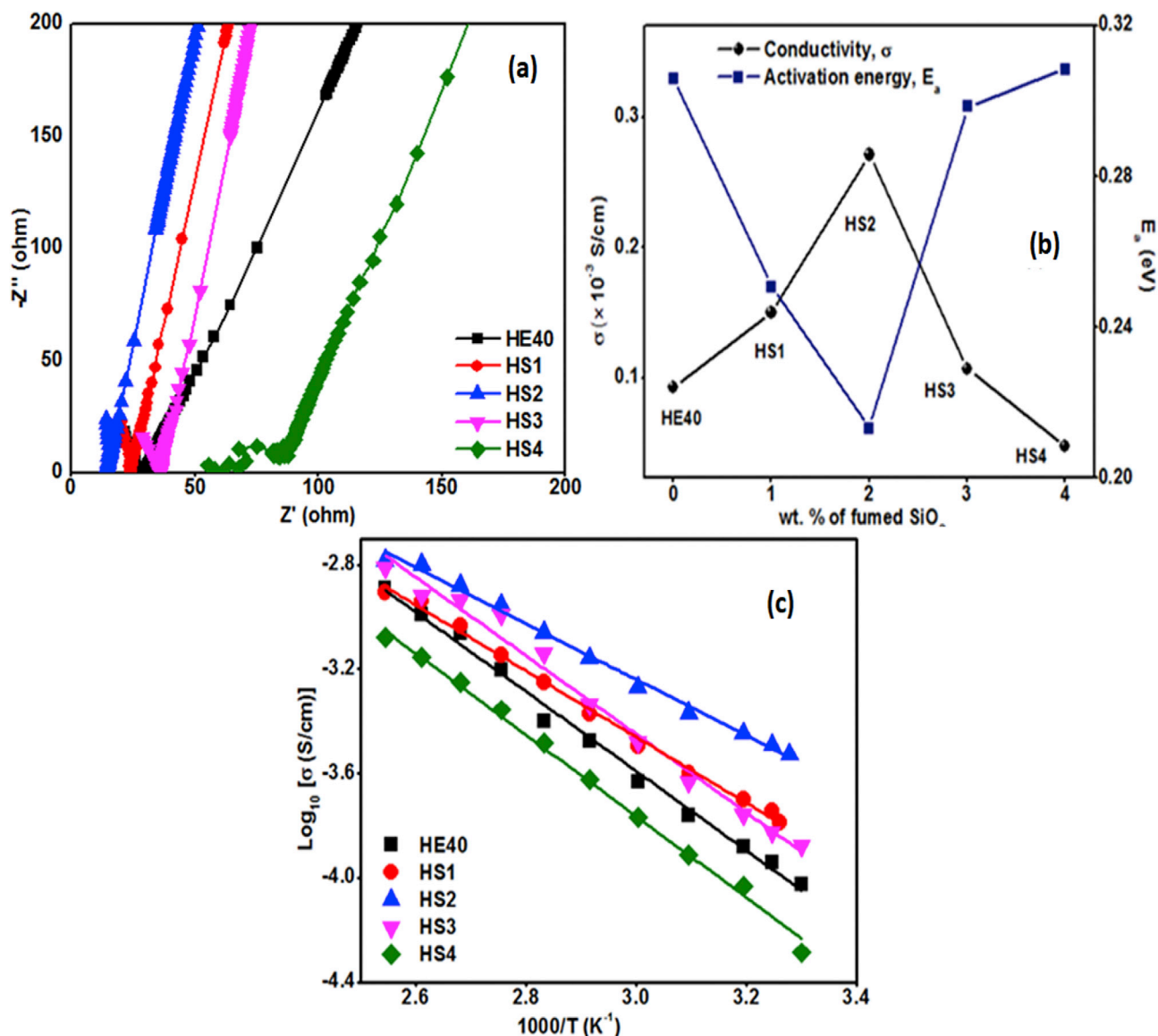


Fig. 1. (a) Cole-Cole plot for SPE complexes at various wt. % of fumed silica nanoparticles at room temperature (b) Variation of ionic conductivity and activation energy at various wt. % of fumed silica nanoparticles at room temperature (c) Variation of logarithm ionic conductivity from 30 to 120 °C at various wt. % of fumed silica nanoparticles.

slurry was formed. This slurry was subsequently coated on the 10 mm diameter coin-shaped stainless steel current collectors and dried in an oven for 8 h at 70 °C.

2.5. Fabrication of symmetric supercapacitor cell

The non-aqueous symmetric EDLC cell was fabricated by sandwiching the SPE film between two activated carbon based electrodes. Thereafter, the cell was pressed by hydraulic hand pump at 0.7 MPa to ensure good contact between the electrode and electrolyte. The EDLC cell configuration was eventually placed in a cell kit for further electrochemical analyses.

2.6. Supercapacitor performance studies

The EDLC cell was subjected to CV, GCD and EIS for electrochemical performance studies by using Gamry Interface 1000 instrument. The CV measurements of EDLC were performed at different scan rates (5, 10, 20,

30, 40 and 50 mV/s) in the potential range between −1 and 1 V. The EIS measurement was done in the frequency range of 10 mHz–100,000 Hz, whereas the GCD was performed at different current densities of 30, 40, 60, 80 and 100 mA/g. The specific capacitance (C_{sp}) of EDLC obtained from CV and GCD was calculated by following equations [19]:

$$C_{sp}(CV) = \frac{A}{\Delta V \times v \times m} \quad (8)$$

$$C_{sp}(GCD) = \frac{I \times \Delta t}{\Delta V \times m} \times 2 \quad (9)$$

Where, A is the integral area of the cyclic voltammogram loop, ΔV is the potential window (V), v is the scan rate (V/s) m is the total mass loading (g) of active material on both electrodes, I is the discharge current and Δt is the discharged time after IR drop. Factor 2 was used in equation (9) because the series capacitance was formed in a two-electrode system.

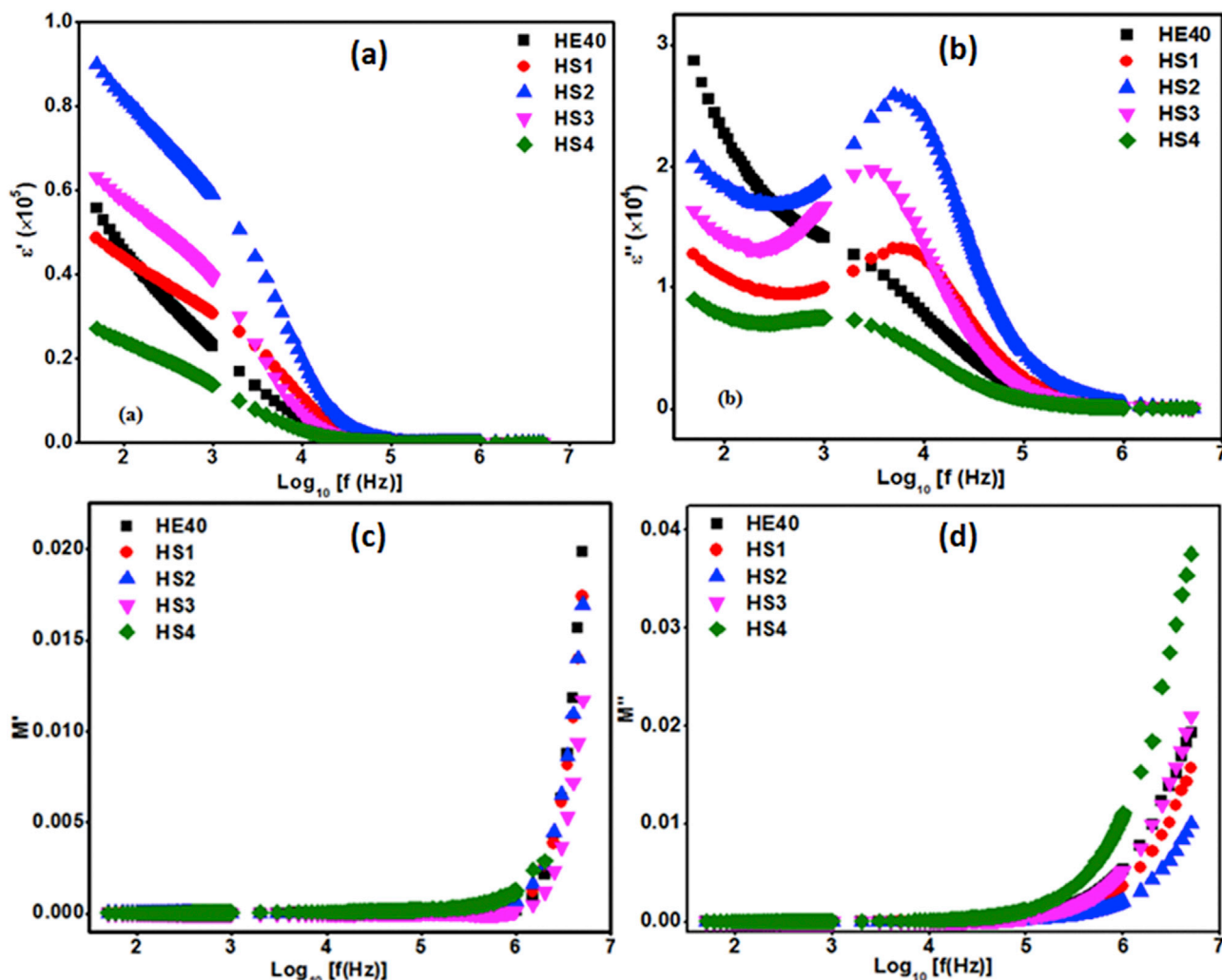


Fig. 2. Variation of (a) ϵ' (b) ϵ'' (c) M' (d) M'' with frequency at various wt. % of fumed silica nanoparticles.

3. Results and discussion

3.1. Ionic conductivity studies

Fig. 1(a) shows the impedance plot of HEC-MgTf₂-EMIMTf SPEs at various wt. % of fumed silica nanoparticles at room temperature. Likewise, incomplete semicircles were observed in all the SPE complexes owing to fast transportation of charge carriers. Additionally, HS2 and HS3 complexes suffered less non-homogeneity at the electrode/electrolyte interface compared to HS1 and HS4 and imply more capacitive behavior because the inclined spike of HS2 and HS3 are closer to the vertical axis [20]. However, HS2 attained the lowest R_b value of 14.5 Ω at high frequency region, followed by HS1 (24.1 Ω), HS3 (36.0 Ω) and HS4 (86.8 Ω). As a consequence, both HS1 and HS2 obtained ionic conductivity of 1.5×10^{-4} S/cm and 2.7×10^{-4} S/cm, respectively at room temperature. On the other hand, both HS3 and HS4 obtained ionic conductivity of 1.1×10^{-4} S/cm and 4.7×10^{-5} S/cm, respectively at room temperature. The calculation of ionic conductivity at room temperature is based on equation (1). The HS2-based SPE achieved the highest ionic conductivity at room temperature by virtue of silanol (Si-OH) group in fumed silica nanoparticles which served as conjunction site with high affinity of charge carriers [21]. On the contrary, both HS3 and HS4 attained a dropped of ionic conductivity by 60.5% and 82.5%, respectively compared to HS2 due to the clustering of nanoparticles which retard the flexibility of the polymer chain [22].

Fig. 1(b) illustrates the relationship between the ionic conductivity

and activation energy at various wt. % of fumed silica nanoparticles at room temperature. The most conducting SPE (HS2) obtained the lowest activation energy of 0.213 eV due to its easiness to hop to vacant spaces while HS1, HS3 and HS4 obtained activation energies of 0.3251 eV, 0.3298 eV and 0.309 eV, respectively by using equation (2).

Fig. 1(c) depicts the linear relationship between variations of logarithm of ionic conductivities with $1000/T$ at various wt. % of fumed silica nanoparticles. Thus, all the SPE complexes obeyed Arrhenius theory. According to Idris et al. (2012), all the SPE complexes were thermally activated because the mobility of charge carriers and expansion of polymer were escalated greatly [23]. Hence, the ions have more opportunities to hop to the vacant spaces provided.

3.2. Dielectric studies

Fig. 2(a) shows the variation of ϵ' against frequencies at various wt. % of fumed silica nanoparticles. Generally, the ϵ' decreases with increasing value of frequencies at various wt. % of fumed silica nanoparticles. At low frequency, HS2 achieved the highest ϵ' (9.0×10^4) by using equation (4) because it has the highest number of ions accumulated near the surface of the stainless steel electrodes which is in well agreement with the EIS result discussed in section 3.1 [24]. Subsequently, at moderate frequency (10^3 – $10^{4.5}$ Hz), the charges were stored in the SPE complexes through the realignment of electric dipoles with the electrical field. At high frequency, all the SPE complexes obtained a steady state of dielectric permittivity because the electric dipoles were unable to obey the

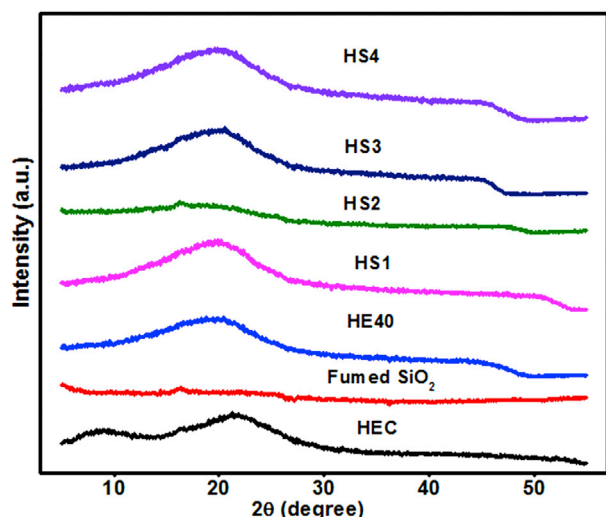


Fig. 3. XRD patterns of pure samples (HEC and fumed silica) and SPE complexes at various wt. % of fumed silica nanoparticles.

variation of high electrical field [25].

Fig. 2(b) describes the variation of ϵ'' against frequencies at various wt. % of fumed silica nanoparticles. The maximum inflection peak of HS2

(the most conducting SPE) has been shifted to the highest frequency of $10^{3.7}$ Hz compared to HS1, HS3, HS4 and HE40 by using equation (5) because HS2 has more ions to relax at a higher frequency region and it experienced the greatest molecular relaxation (orientation and polarization) [26].

Fig. 2(c) and (d) show the variation of M' and M'' against frequencies, respectively at various wt. % of fumed silica nanoparticles. Both the M' and M'' were calculated based on Equations (6) and (7), respectively. The M' and M'' for all SPE complexes portrayed a “long-tail” pattern from low frequency to $10^{5.5}$ Hz and 10^5 Hz, respectively. The applied electrical field on the long-range ionic conductivity for all SPE complexes were insignificant because this type of conductivity is independent from the nature of electrode materials, the contact between electrode/electrolyte interface, and the impurities adsorbed on the polymer electrolytes. Additionally, all the SPE complexes do not showed maximum peak proving that SPE films are ionic conductor because the experimental frequency window is narrow [27].

3.3. XRD studies

Fig. 3 demonstrates the XRD patterns of pure samples (HEC and fumed silica nanoparticles) and SPE complexes at various wt. % of fumed silica nanoparticles. All the SPEs (without and with incorporation of fumed silica nanoparticles) attained a complexation peak at $2\theta = 20.0^\circ$. Among all the SPEs, HS2 experienced an abrupt decrease in peak broadness at $2\theta = 20.0^\circ$ by 53.4% compared to HE40. According to

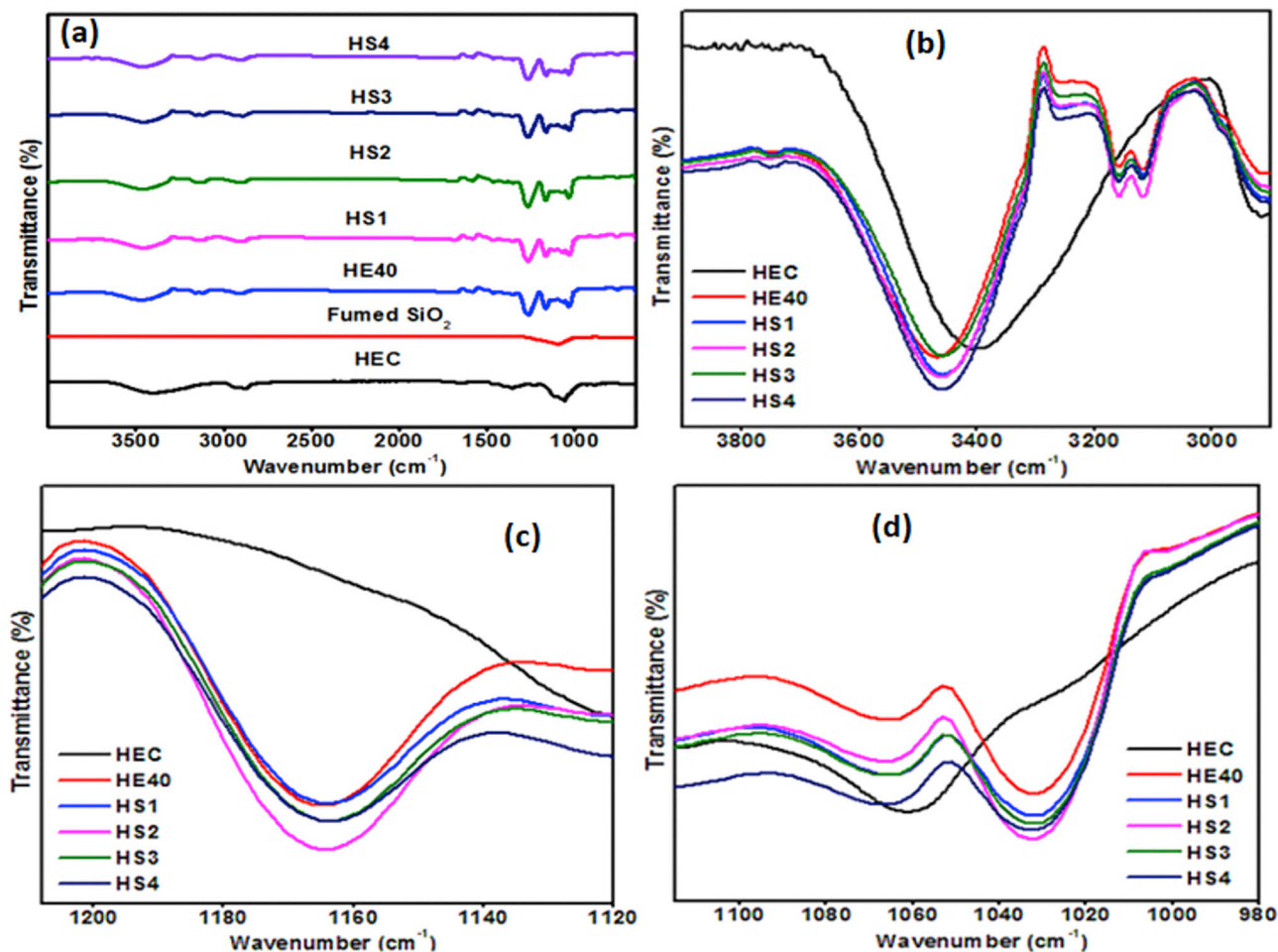


Fig. 4. (a) FTIR spectra of pure samples (HEC and fumed silica) and SPE complexes at various wt. % of fumed silica nanoparticles (b) The interactions in the SPE complexes (without and with fumed silica nanoparticles) at $-\text{OH}$ stretching (3473 cm^{-1}) (c) The interactions in the SPE complexes (without and with fumed silica nanoparticles) at SO_2 symmetric stretching of CF_3SO_3^- (1165 cm^{-1}) (d) The interactions in the SPE complexes (without and with fumed silica nanoparticles) at asymmetric in-plane C–O–C pyroxy ring stretching (1030 cm^{-1}).

Table 2

Band assignments of pure samples (HEC and fumed silica nanoparticles) and SPE complexes at various wt. % of fumed silica nanoparticles.

Band assignments	HEC (cm ⁻¹)	Fumed silica (cm ⁻¹)	HE40 (cm ⁻¹)	HS1 (cm ⁻¹)	HS2 (cm ⁻¹)	HS3 (cm ⁻¹)	HS4 (cm ⁻¹)	Reference
Asymmetric –CH ₂ and –CH ₃ stretching	2917	–	2923	2923	2926	2923	2917	[32]
Symmetric –CH ₂ and –CH ₃ stretching	2876	–	2881	2887	2887	2884	2884	[32]
–OH in-plane bending	1239	–	1260	1251	1254	1254	1251	[33]
Asymmetric out-of-phase C–O–C pyrore ring stretching	889	–	862	889	889	889	892	[33]

Table 3The decomposition temperature of pure samples (HEC, MgTf₂ and EMIMTf) and SPE complexes at various wt. % of fumed silica nanoparticles.

Samples	Thermal decomposition (C)			
	Stage 1	Stage 2	Stage 3	Stage 4
HEC	295.9	–	–	–
MgTf ₂	107.2	460.5	–	–
EMIMTf	397.5	–	–	–
HE40	51.8	266.6	382.9	466.0
HS1	88.0	282.3	395.3	472.3
HS2	88.0	276.9	414.9	475.9
HS3	88.0	278.7	418.5	475.9
HS4	88.0	284.1	420.3	477.7

Burgaz (2011), the crystallinity of the host polymer destroyed when an optimum amount of amorphous nanoparticles are incorporated into the SPE [28]. Thus, ample spaces for adsorption of charge carriers were provided and led to the escalation of ionic conductivity as discussed in section 3.1.

3.4. FTIR studies

Fig. 4(a) depicts the FTIR spectra of pure samples (HEC and fumed silica nanoparticles) and SPE complexes at various wt. % of fumed silica nanoparticles. Fumed silica nanoparticles has an intense and broad characteristic peaks at 1086 cm⁻¹ and 806 cm⁻¹ that are responsible for asymmetric and symmetric vibrations of Si–O–Si, respectively [29]. However, the characteristic peaks of fumed silica nanoparticles were not noticeable in HS1, HS2, HS3 and HS4 due to very little amount of fumed silica nanoparticles incorporated into HE40.

Despite, a minor decrease in the broadness of –OH stretching (3473 cm⁻¹) was due to incorporation of fumed silica nanoparticles into the HEC-MgTf₂-EMIMTf complexes. The broadness of the SPE complexes

incorporated with fumed silica nanoparticles depressed by 40.8% compared to HE40 as shown in Fig. 4(b). In the same manner, the bending of in-plane –OH (1239 cm⁻¹) has been shifted to a higher wavenumber with respect to HE40. This is owing to the destruction of intermolecular hydrogen bonding formed among silanol group in fumed silica nanoparticles, host polymer and between fumed silica nanoparticles and host polymer [30]. Additionally, the spaces between host polymer were fill up by small size of silica nanoparticles and thereby ion-dipole forces between Si⁴⁺ and lone pair electrons on the oxygen atom of the host polymer become more remarkable than intermolecular hydrogen bonding [31].

Fig. 4(c) and (d) demonstrate the SO₂ symmetric stretching of CF₃SO₃⁻ and in-plane C–O–C pyrore ring stretching at 1165 cm⁻¹ and 1030 cm⁻¹, respectively. HS2 exhibited vigorous interaction with charge carriers through the significant decrease in peak intensity by 34.7% at wavenumber 1030 cm⁻¹ (asymmetric in-plane of C–O–C pyrore ring stretching) which was attributed to the adsorption of Mg²⁺ ions (cation) on the host polymer. On the other hand, the least change in peak intensity by 8.9% at wavenumber 1165 cm⁻¹ (SO₂ symmetric stretching of CF₃SO₃⁻) was in lieu to the adsorption of CF₃SO₃⁻ ions (anion) on the fumed silica nanoparticles. Instead of these changes, prominent changes in wavenumber were observed at peaks 2923 cm⁻¹ (asymmetric –CH₂ and –CH₃ stretching), 2881 cm⁻¹ (symmetric –CH₂ and –CH₃ stretching), 1357 cm⁻¹ (C–H bending of –CH₂ and –CH₃) and 862 cm⁻¹ (asymmetric out-of-phase C–O–C pyrore ring stretching) as summarize in Table 2.

3.5. TGA studies

Table 3 portrays the decomposition temperature of pure samples (MgTf₂, EMIMTf and HEC) and SPE complexes at various wt. % of fumed silica nanoparticles. Fig. 5(a) shows the thermogram of pure samples (MgTf₂, EMIMTf, HEC and fumed silica nanoparticles), whereas Fig. 5(b) depicts the thermogram of SPE complexes at various wt. % of fumed silica

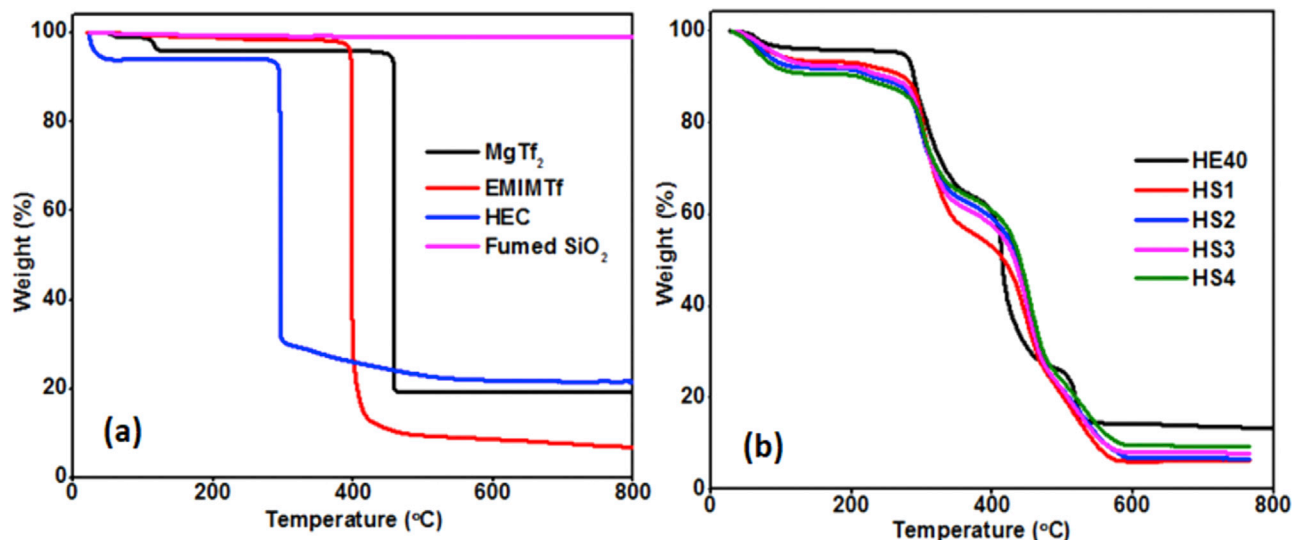


Fig. 5. Thermograms of (a) pure samples (HEC, MgTf₂, EMIMTf and fumed silica nanoparticles) (b) SPE complexes at various wt. % of fumed silica nanoparticles.

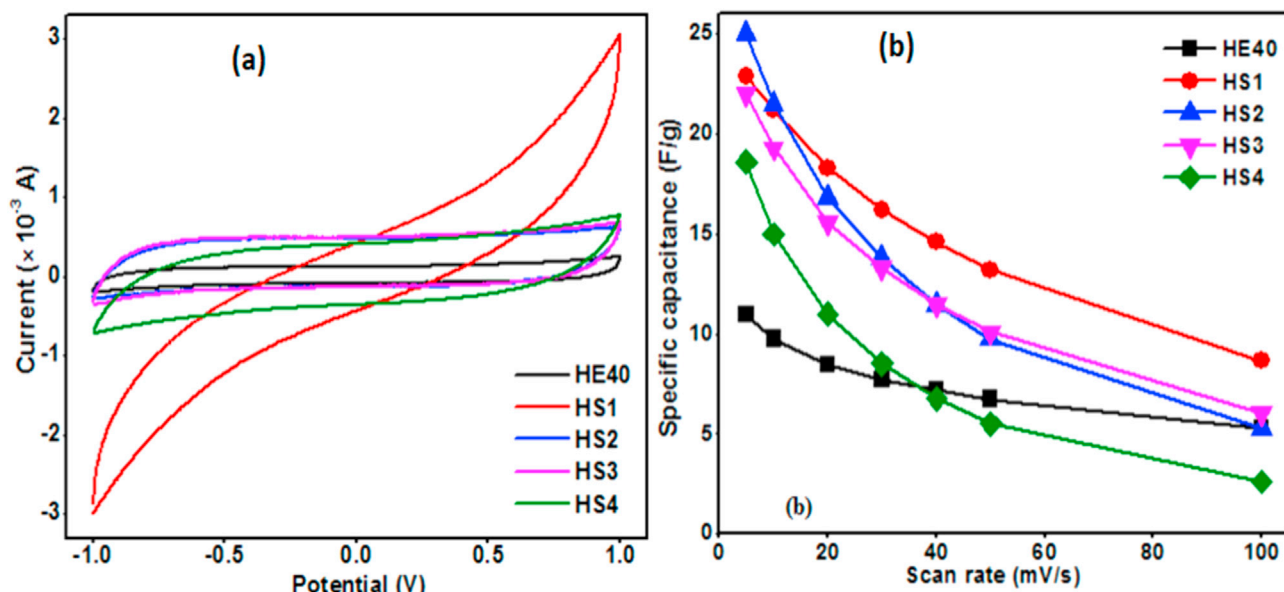


Fig. 6. (a) CV responses at scan rate of 5 mV/s for EDLC cells (without and with incorporation of fumed silica nanoparticles) (b) Specific capacitance for EDLC cells (without and with incorporation of fumed silica nanoparticles) as a function of scan rate.

nanoparticles. Based on Fig. 5(a), pure fumed silica nanoparticles did not show any weight loss due to the high decomposition temperature of silica nanoparticles (which was beyond the measuring limit of the instrument). Generally, the thermal stability of all the SPE complexes improved upon incorporation of fumed silica nanoparticles which was indicated by the enhancement in decomposition temperature at stage 4. Additionally, all the SPE complexes facing shifts in decomposition temperature compared to pure samples due to complexation between the host polymer and adsorbed ions in the samples as discussed in sections 3.3 and 3.4 [34]. The decomposition temperature at stage 4 (466.0–478.0 °C) was owing to the decomposition of MgTf_2 whereas the decomposition temperature at stage 3 (382.0–420.0 °C) and stage 2 (266.0–284.0 °C) were responsible for the decomposition of EMIMTf and HEC, respectively. At early stage, HE40 suffered 4.1% weight loss at decomposition temperature of 54.0 °C due to evaporation of volatile minor impurities and absorbed moisture [35].

3.6. Cyclic voltammetry studies

Fig. 6(a) demonstrates the CV responses for EDLCs at scan rate of 5 mV/s. It was found that the maximum specific capacitance calculated based on equation (8) were 23 F/g, 25 F/g, 22 F/g and 19 F/g upon incorporation of 1, 2, 3 and 4 wt. % of fumed silica nanoparticles into HE40. HS2-based cell attained the highest increase in specific capacitance at scan rate of 5 mV/s by 127.3% compared to HE40 cell (11 F/g). Interestingly, all the samples demonstrate an excellent double layer capacitive characteristics below scan rate of 50 mV/s which is evident from the rectangular shape of their CV curve without showing any oxidation or reduction peak. Fig. 6(b) depicts the variation of specific capacitance of EDLCs as a function of scan rate. The specific capacitance for all the EDLCs decreased with increasing scan rate due to the delay in reverse adsorption of ions on the electrode/electrolyte interface which is also known as “Electrolyte Starvation Effect” [36]. The phenomena were supported by the distorted leaf like shape of the CV curve (without and with fumed silica nanoparticles) at scan rate of 100 mV/s.

As a result, the performance of the EDLCs with incorporation of fumed silica nanoparticles were better than HE40 because the charge carriers adsorbed on the fumed silica nanoparticles permeates faster than the ions adsorbed on the host polymer (bulky molecules) into the carbon electrodes [37]. Among the EDLCs incorporated with fumed silica

nanoparticles, HS2-based cell achieved the highest maximum specific capacitance compared to its counterparts due to the successful penetration of large number of ions into the carbon electrodes. This was due to HS2-based SPE possessed the highest number of mobile charge carriers which smoothen the penetration of ions into the carbon electrodes [38].

3.7. EIS studies

Table 4 and Fig. 7 demonstrate the R_{ct} values and electrochemical impedance spectra of EDLC cells (without and with incorporation of

Table 4

R_{ct} values for EDLC cells (with and without incorporation of fumed silica nanoparticles).

EDLC cell	R_{ct} (Ω)
HE40	142.0
HS1	59.8
HS2	47.4
HS3	78.8
HS4	132.3

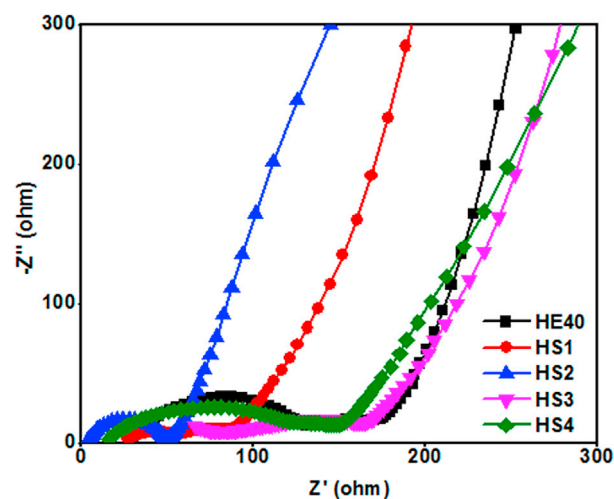


Fig. 7. Electrochemical impedance spectra of EDLC cells (without and with incorporation of fumed silica nanoparticles) at room temperature.

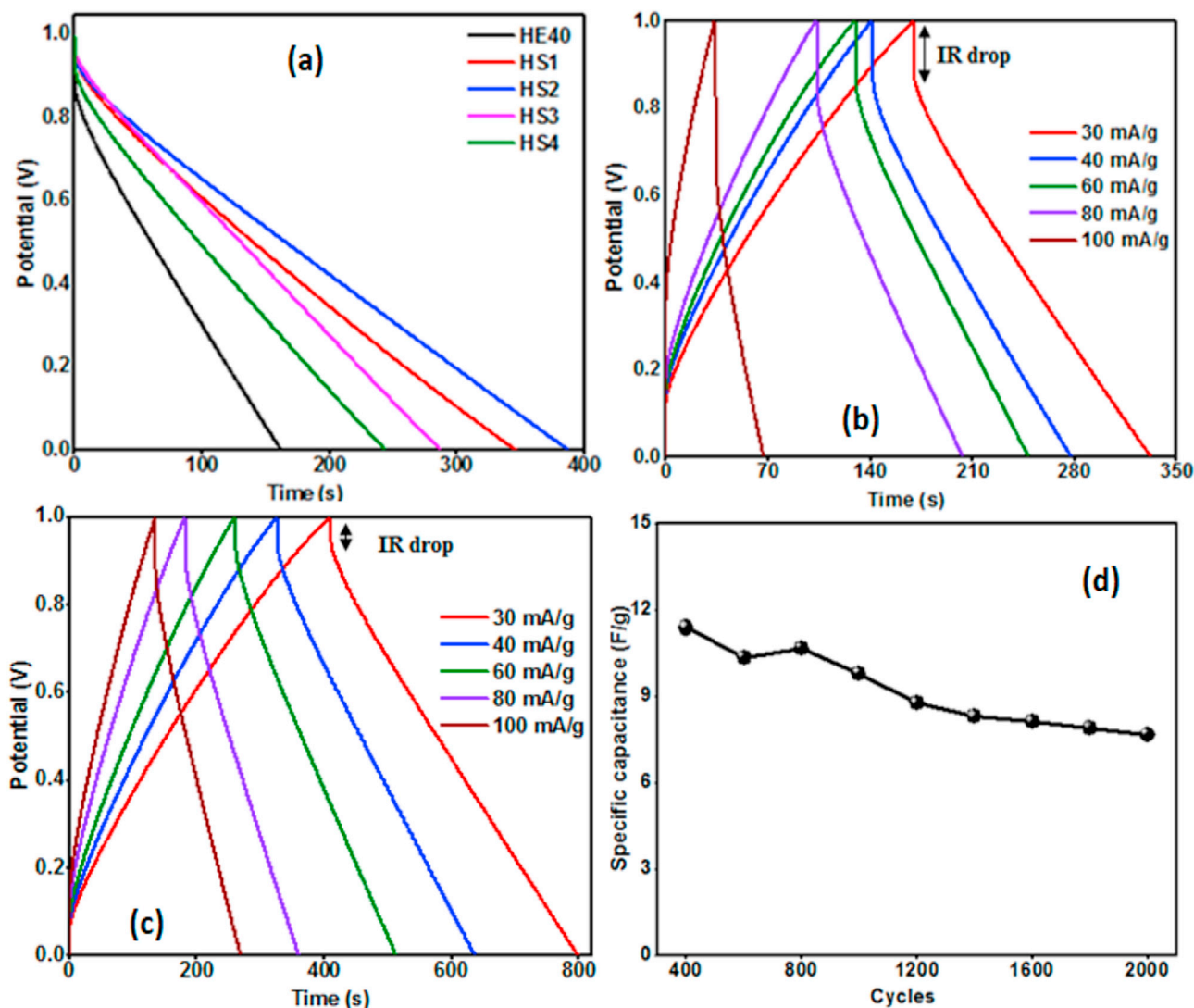


Fig. 8. (a) Discharge curves of EDLC cells (with and without incorporation of fumed silica nanoparticles) at current density of 30 mA/g (b) Galvanostatic charge-discharge curves of HE40 at different current densities (c) Galvanostatic charge-discharge curves of HS2 at different current densities (d) Specific capacitance of HS2-based EDLC over 1600 cycles at current density of 0.4 A/g.

fumed silica nanoparticles) at room temperature, respectively.

Generally, the charge transfer resistance values for all the EDLC cells after incorporated with fumed silica nanoparticles were lesser than HE40-based cell. The HS2-based SPE achieved the highest ionic conductivity at room temperature as well as maximum specific capacitance, thus it attained the lowest R_{ct} value (47.4 Ω). This phenomena signified that minimum resistance was created by HS2-based cell due to its thickness along with good transportation of Mg^{2+} ions into the carbon electrodes [39]. The results obtained are in well agreement with the maximum specific capacitance calculated at 5 mV/s and the ionic conductivities measured at room temperature which were discussed in sections 3.5 and 3.1, respectively.

3.8. GCD studies

Fig. 8(a) demonstrates the discharge curves of EDLCs at current density of 30 mA/g. Based on the plot, HS1, HS2, HS3 and HS4 based cells achieved longer discharge time of 347.8 s, 389.0 s, 288.6 s, 245.5 s, respectively compared to HE40 cell (136.3 s). Consequently, HS2 cell exhibits the best discharge property owing to its' longest discharge time by 185.4% compared to HE40 cell because HS2-based SPE provided more Mg^{2+} ions, which diffused deeply and adsorbed strongly to the carbon

electrodes. Likewise, HS2-based cell obtained the highest specific capacitance (24.6 F/g) while HE40, HS1, HS3 and HS4 cells obtained specific capacitance of 9.5 F/g, 22.9 F/g, 22.0 F/g and 18.6 F/g, respectively at current density of 30 mA/g using equation (9). It was found that the EDLCs incorporated with fumed silica nanoparticles possess higher specific capacitance than HE40 cell and these values resemble the specific capacitance calculated by CV curves.

Fig. 8(b) and (c) depict the galvanostatic charge-discharge curve in the potential range of 0–1 V at different current densities (30, 40, 60, 80 and 100 mA/g) for HE40 and HS2, respectively. Both HS2 and HE40 based EDLCs showed the occurrence of non-Faradaic process because they achieved symmetric triangles of galvanostatic charge-discharge curve [40]. Moreover, the internal build-up resistance in the cell depleted upon incorporation of fumed silica nanoparticles resulted from less ohmic drop (IR drop).

Generally, the performance of EDLCs improved greatly upon incorporation of fumed silica nanoparticles because the diffusion of ions on the electrode/electrolyte interfacial contact was facilitated by small particle size of fumed silica nanoparticles. Nevertheless, all the EDLCs suffered from depletion of specific capacitance at higher current densities which implies its poor rate performance. Similarly, the IR drop values for all EDLCs elevated at higher current densities because the stability of

Table 5

Comparison of specific capacitances and capacitance retention for HS2 cell from the previous literature.

Electrolyte	Electrode	Specific capacitance from CV curve (F/g)	Scan rate (mV/s)	Current density	Cycle number	Capacitance retention (%)	References
Methyl cellulose (solid)	AC	38.0	1	1 mA	4	–	[42]
Corn starch (solid)	AC	8.7	10	1 mA	500	–	[43]
Corn starch (solid)	AC	36.8	10	1 mA	500	–	[44]
PVA (solid)	AC	2.0	10	1 mA	–	–	[45]
HEC (solid)	AC	21.4	5	0.4 A/g	3000	91.3	[46]
Poly(ϵ -caprolactone)	AC	42.4	10	–	–	–	[47]
Acrylic acid (liquid)	AC	24.01	5	–	4000	97.7%	[48]
Poly(vinylidene fluoride-co-hexafluoropropylene)	AC	29.6	3	0.2 A/g	3000	94%	[34]
HEC (solid)	AC	25.0	5	0.4 A/g	1600	71.3%	This work

polymer electrolyte shattered [41]. Subsequently, HS2-based SPE was selected for the fabrication of EDLC to test its stability at current density of 0.4 A/g. The capacitance of the cell can withstand 71.3% from its initial capacitance over 1600 cycles at current density of 0.4 A/g as depicted in Fig. 8(d). The life cycle test and the specific capacitance by HS2 cell was compared to the results found in the previous literature, which are summarized in Table 5.

4. Conclusions

SPEs (with and without incorporation of fumed silica nanoparticles) are prepared using solution casting technique. These SPEs are characterized and it is found that the SPE doped with 2 wt. % of fumed silica nanoparticles achieves the highest ionic conductivity (2.7×10^{-4} S/cm) at room temperature along with the great reduction of crystallinity at peak $2\theta = 20.0^\circ$ by 53.4%. The results are well supported by the decrease in $-\text{OH}$ stretching (3473 cm^{-1}) by 40.8%. Nevertheless, the enhancement in adsorption of ions by the nanoparticles on the polymer backbone were equipped with high dielectric permittivity value (9.0×10^4) and low activation energy of 0.213 eV. Also, it is proven through great adsorptions of both Mg^{2+} and CF_3SO_3^- ions on the host polymer at wavenumber of 1030 cm^{-1} (asymmetric in-plane of C–O–C pyrore ring stretching) and 1165 cm^{-1} (SO_2 symmetric stretching of CF_3SO_3^-), respectively. Additionally, the thermal stability of the SPEs improved upon incorporation of fumed silica nanoparticles. Hence, good performance of EDLCs are predominant. The most performing cell is HS2-based EDLC because it is able to withstand 71.3% of capacitance from its initial capacitance value over 1600 cycles at current density of 0.4 A/g.

Acknowledgements

This work is financially supported by University of Malaya Research Grant (UMRG: RG382-17AFR). The authors would like to thank MyPhD for their scholarship, Universiti Malaya Research Grant IPPP (Project Account Number: PG030-2015A) and INTI International University, Nilai for their technical support.

References

- [1] S. Orlins, D. Guan, China's toxic informal e-waste recycling: local approaches to a global environmental problem, *J. Clean. Prod.* 114 (2016) 71–80.
- [2] F. Suja, R. Abdul Rahman, A. Yusof, M.S. Masdar, e-Waste management scenarios in Malaysia, *J. Waste Manag.* 2014 (2014).
- [3] M. Heacock, C.B. Kelly, W.A. Suk, E-waste: the growing global problem and next steps, *Rev. Environ. Health* 31 (2016) 131–135.
- [4] S. Stianopkiao, M.H. Wong, Handling e-waste in developed and developing countries: initiatives, practices, and consequences, *Sci. Total Environ.* 463 (2013) 1147–1153.
- [5] Z. Sun, Y. Xiao, J. Sietsma, H. Agterhuis, Y. Yang, A cleaner process for selective recovery of valuable metals from electronic waste of complex mixtures of end-of-life electronic products, *Environ. Sci. Technol.* 49 (2015) 7981–7988.
- [6] P. Simon, Y. Gogotsi, Materials for electrochemical capacitors, *Nat. Mater.* 7 (2008) 845–854.
- [7] F.S. Omar, A. Numan, N. Duraisamy, S. Bashir, K. Ramesh, S. Ramesh, A promising binary nanocomposite of zinc cobaltite intercalated with polyaniline for supercapacitor and hydrazine sensor, *J. Alloy. Comp.* 716 (2017) 96–105.
- [8] C.C. Lee, F.S. Omar, A. Numan, N. Duraisamy, K. Ramesh, S. Ramesh, An enhanced performance of hybrid supercapacitor based on polyaniline-manganese phosphate binary composite, *J. Solid State Electrochem.* (2017) 1–9.
- [9] I. Stepniak, M. Galinski, K. Nowacki, M. Wysokowski, P. Jakubowska, V.V. Bazhenov, T. Leisegang, H. Ehrlich, T. Jesionowski, A novel chitosan/sponge chitin origin material as a membrane for supercapacitors—preparation and characterization, *RSC Adv.* 6 (2016) 4007–4013.
- [10] Y. Yusof, N. Majid, R. Kasmani, H. Illias, M. Kadir, The effect of plasticization on conductivity and other properties of starch/chitosan blend biopolymer electrolyte incorporated with ammonium iodide, *Mol. Cryst. Liq. Cryst.* 603 (2014) 73–88.
- [11] S. Chahal, F.S.J. Hussain, A. Kumar, M.S.B.A. Rasad, M.M. Yusoff, Fabrication, characterization and in vitro biocompatibility of electrospun hydroxyethyl cellulose/poly (vinyl) alcohol nanofibrous composite biomaterial for bone tissue engineering, *Chem. Eng. Sci.* 144 (2016) 17–29.
- [12] K. Mahmoud, Optical properties of hydroxyethyl cellulose film treated with nitrogen plasma, *Spectrochim. Acta Part A Mol. Biomol. Spectrosc.* 157 (2016) 153–157.
- [13] C.-W. Liew, H. Ng, A. Numan, S. Ramesh, Poly (acrylic acid)-based hybrid inorganic-organic electrolytes membrane for electrical double layer capacitors application, *Polymers* 8 (2016) 179.
- [14] I.A. Rahman, V. Padavettan, Synthesis of silica nanoparticles by sol-gel: size-dependent properties, surface modification, and applications in silica-polymer nanocomposites—a review, *J. Nanomater.* 2012 (2012) 8.
- [15] S.H. Kim, S.H. Ahn, T. Hirai, Crystallization kinetics and nucleation activity of silica nanoparticle-filled poly (ethylene 2, 6-naphthalate), *Polymer* 44 (2003) 5625–5634.
- [16] S. Ramesh, C.-W. Liew, Exploration on nano-composite fumed silica-based composite polymer electrolytes with doping of ionic liquid, *J. Non-Cryst. Solids* 358 (2012) 931–940.
- [17] D. Tang, R. Yuan, Y. Chai, Magnetic control of an electrochemical microfluidic device with an arrayed immunosensor for simultaneous multiple immunoassays, *Clin. Chem.* 53 (2007) 1323–1329.
- [18] M.T. Taghizadeh, P. Seifi-Aghjehkhal, Sonocatalytic degradation of 2-hydroxyethyl cellulose in the presence of some nanoparticles, *Ultrason. Sonochem.* 26 (2015) 265–272.
- [19] C. Xiang, M. Li, M. Zhi, A. Manivannan, N. Wu, A reduced graphene oxide/Co 3 O 4 composite for supercapacitor electrode, *J. Power Sources* 226 (2013) 65–70.
- [20] S. Rajendran, R.S. Babu, P. Sivakumar, Effect of salt concentration on poly (vinyl chloride)/poly (acrylonitrile) based hybrid polymer electrolytes, *J. Power Sources* 170 (2007) 460–464.
- [21] S.B. Aziz, Z.H.Z. Abidin, Electrical conduction mechanism in solid polymer electrolytes: new concepts to arrhenius equation, *J. Soft Matter* 2013 (2013).
- [22] Y.-J. Wang, D. Kim, Crystallinity, morphology, mechanical properties and conductivity study of in situ formed PVdF/LiClO 4/TiO 2 nanocomposite polymer electrolytes, *Electrochim. Acta* 52 (2007) 3181–3189.
- [23] N.H. Idris, M.M. Rahman, J.-Z. Wang, H.-K. Liu, Microporous gel polymer electrolytes for lithium rechargeable battery application, *J. Power Sources* 201 (2012) 294–300.
- [24] R. Mishra, K. Rao, Electrical conductivity studies of poly (ethyleneoxide)-poly (vinylalcohol) blends, *Solid State Ionics* 106 (1998) 113–127.
- [25] B.M. Tareev, Physics of Dielectric Materials, Mir publishers, 1975.
- [26] P. Tamilselvi, M. Hema, Conductivity studies of LiCF 3 SO 3 doped PVA: PVdF blend polymer electrolyte, *Phys. B Condens. Matter* 437 (2014) 53–57.
- [27] M. Dasari, K.S. Rao, P.M. Krishna, G.G. Krishna, Barium strontium bismuth niobate layered perovskites: dielectric, impedance and electrical modulus characteristics, *Acta Phys. Pol. A* 119 (2011) 387–394.
- [28] E. Burgaz, Poly (ethylene-oxide)/clay/silica nanocomposites: morphology and thermomechanical properties, *Polymer* 52 (2011) 5118–5126.
- [29] Y.-D. Huang, X.-D. Gao, Z.-Y. Gu, X.-M. Li, Amino-terminated SiO 2 aerogel towards highly-effective lead (II) adsorbent via the ambient drying process, *J. Non-Cryst. Solids* 443 (2016) 39–46.
- [30] M.K. Gupta, Y.-C. Tseng, D. Goldman, R.H. Bogner, Hydrogen bonding with adsorbent during storage governs drug dissolution from solid-dispersion granules, *Pharmaceut. Res.* 19 (2002) 1663–1672.

- [31] T. Tanaka, G. Montanari, R. Mulhaupt, Polymer nanocomposites as dielectrics and electrical insulation-perspectives for processing technologies, material characterization and future applications, *IEEE Trans. Dielectr. Electr. Insul.* 11 (2004) 763–784.
- [32] N. Abidi, L. Cabrales, C.H. Haigler, Changes in the cell wall and cellulose content of developing cotton fibers investigated by FTIR spectroscopy, *Carbohydr. Polym.* 100 (2014) 9–16.
- [33] C. Chung, M. Lee, E.K. Choe, Characterization of cotton fabric scouring by FT-IR ATR spectroscopy, *Carbohydr. Polym.* 58 (2004) 417–420.
- [34] N. Fattah, H. Ng, Y. Mahipal, A. Numan, S. Ramesh, K. Ramesh, An approach to solid-state electrical double layer capacitors fabricated with graphene oxide-doped, ionic liquid-based solid copolymer electrolytes, *Materials* 9 (2016) 450.
- [35] C.-W. Liew, S. Ramesh, A. Arof, Characterization of ionic liquid added poly (vinyl alcohol)-based proton conducting polymer electrolytes and electrochemical studies on the supercapacitors, *Int. J. Hydrogen Energy* 40 (2015) 852–862.
- [36] R. Mysyk, E. Raymundo-Pinero, F. Béguin, Saturation of subnanometer pores in an electric double-layer capacitor, *Electrochem. Commun.* 11 (2009) 554–556.
- [37] R. Chandrasekaran, Y. Soneda, J. Yamashita, M. Kodama, H. Hatori, Preparation and electrochemical performance of activated carbon thin films with polyethylene oxide-salt addition for electrochemical capacitor applications, *J. Solid State Electrochem.* 12 (2008) 1349–1355.
- [38] G. Gryglewicz, J. Machnikowski, E. Lorenc-Grabowska, G. Lota, E. Frackowiak, Effect of pore size distribution of coal-based activated carbons on double layer capacitance, *Electrochim. Acta* 50 (2005) 1197–1206.
- [39] P. Taberna, P. Simon, J.-F. Fauvarque, Electrochemical characteristics and impedance spectroscopy studies of carbon-carbon supercapacitors, *J. Electrochem. Soc.* 150 (2003) A292–A300.
- [40] N. Nadiyah, Y. Mahipal, A. Numan, S. Ramesh, K. Ramesh, Efficiency of supercapacitor using EC/DMC-based liquid electrolytes with methyl methacrylate (MMA) monomer, *Ionics* 22 (2016) 107–114.
- [41] B. Xu, F. Wu, S. Chen, C. Zhang, G. Cao, Y. Yang, Activated carbon fiber cloths as electrodes for high performance electric double layer capacitors, *Electrochim. Acta* 52 (2007) 4595–4598.
- [42] N. Shuhaimi, L. Teo, H. Woo, S. Majid, A. Arof, Electrical double-layer capacitors with plasticized polymer electrolyte based on methyl cellulose, *Polym. Bull.* 69 (2012) 807–826.
- [43] K. Teoh, C.-S. Lim, C.-W. Liew, S. Ramesh, Electric double-layer capacitors with corn starch-based biopolymer electrolytes incorporating silica as filler, *Ionics* 21 (2015) 2061–2068.
- [44] C.-W. Liew, S. Ramesh, Electrical, structural, thermal and electrochemical properties of corn starch-based biopolymer electrolytes, *Carbohydr. Polym.* 124 (2015) 222–228.
- [45] C.-W. Liew, S. Ramesh, A. Arof, Investigation of ionic liquid-doped ion conducting polymer electrolytes for carbon-based electric double layer capacitors (EDLCs), *Mater. Des.* 92 (2016) 829–835.
- [46] M.Y. Chong, A. Numan, C.W. Liew, K. Ramesh, S. Ramesh, Comparison of the performance of copper oxide and yttrium oxide nanoparticle based hydroxylethyl cellulose electrolytes for supercapacitors, *J. Appl. Polym. Sci.* 134 (2017).
- [47] H. Woo, C.-W. Liew, S. Majid, A. Arof, Poly (ϵ -caprolactone)-based polymer electrolyte for electrical double-layer capacitors, *High Perform. Polym.* 26 (2014) 637–640.
- [48] N. Nadiyah, F.S. Omar, A. Numan, Y. Mahipal, S. Ramesh, K. Ramesh, Influence of acrylic acid on ethylene carbonate/dimethyl carbonate based liquid electrolyte and its supercapacitor application, *Int. J. Hydrogen Energy* 42 (2017) 30683–30690.